nature methods

Article

https://doi.org/10.1038/s41592-023-01836-9

Neural engineering with photons as synaptic transmitters

In the format provided by the authors and unedited

Contents

1 Supplementary Text 1: Considerations for building PhaST

Estimates for photon budget and light sensitivity The number of available channelrhodopsin molecules necessary for neuronal depolarization of mammalian neurons was previously estimated to be in the order of 1 million[1]. How do our results compare with this estimate? We calculated the anticipated and required photon budget to depolarize the postsynaptic neuron sufficiently to evoke signal propagation via light-activated channels. We first estimated how many photons we will obtain given a certain luciferase concentration and synapse volume. Using published values for quantum yield (10/s)[2] and typical overexpression concentrations (10^{-6}M or 3000 molecules) in a synapse with a radius of 0.5μm ($\approx$0.5fL), we expect to obtain approx. 30000 photons/s/synapse. Since a typical calcium transient in ASH in our experiments lasts about $>>$5s (Fig. 1) and ASH forms $\approx$31 synapses with AVA and AIB (Extended Data Fig. 1, Ref. [3]), we expect to have $\approx 4.5 \cdot 10^6$ photons available for stimulation, or 2pW. Because the synaptic cleft is less than the wavelength of the light, we assume there is neither absorption nor scattering, such that this value corresponds to a photon flux of 0.7µW/mm^2 through the postsynaptic membrane halfspace. Because not all photons are emitted in direction of the target cell, this value is overestimated by a factor that depends on the area overlap in the synaptic contact.

To better understand the operational light sensitivity of a real world experiment, we carefully titrated decreasing light levels on freely moving animals expressing ChR2-HRDC in AVA and AIB. We then extrapolated the data with a binary logistic regression model to estimate the response probability at the lowest light intensities (Fig. 2f). With this approach, we inferred that animals still responded at intensities below 1 fW/μm^2. For comparison, because a single photon carries an energy of 1e-19 J, responses at the lowest light intensities used here were evoked with fewer than 10.000 photons$\cdot$s$^{-1}\mu$m^{-2}.

To calculate the relative photon absorption E of the ChR2 in the membrane we apply Lambert-

Beer's law, which relates the path length d (thickness of the membrane/channelrhodopsin), the concentration of absorbers c and extinction coefficient ϵ (1-photon absorbance cross section, 50000 L mol^{-1} cm^{-1} for ChR2; [4]). With reasonable values of the surface area of a synapse of $1\mu m^2$ and an estimated density of 190 molecules/μ m [5], we estimate the concentration of ChR2-HRDC of 62μM within the postsynaptic membrane. Subsequently, according to Lambert-Beer ($E = c \cdot \epsilon \cdot d$) the relative photon absorption is $E = 3.6 \cdot 10^{-6}$, meaning that the intensity of the light after passing through the membrane with ChR2 is $I_0 \cdot 10^E$ and, consequently, ≈4 out of 1 million photons will be absorbed. Because the photon absorption vs. activation ratio of ChR2 is 0.7 [4], we estimate the quantum efficiency of the system is $2.5 \cdot 10^{-4}$ %. Taken together, given the 4.5*10^6 photons emitted from the Nanolantern, we expect to activate >20 channels during a typical stimulation. Because ChR2-XXL is 200 times more sensitive than ChR2[5], the real number is likely much higher.

How many open channels are necessary to depolarize the neuronal membrane for a given amount in a given time? We consider published values of the resting potential of -50mV for AIB[6] and -30mV for AVA[7] and asked how many charges are necessary to depolarize AVA for 20mV, a hypothetical value to activate voltage gated Ca^{2+} channels. Note, AIB is not known to express low threshold T-type calcium channels (e.g. CCA-1) that would activate at lower membrane potentials (-30mV for NMJ, [8]), whereas AVA expresses both, T-type and L-type voltage gated Ca^{2+} channels[9]. Given an input resistance of 5 GOhm, a current of 5pA is necessary to do so. Assuming a specific capacitance of $1\mu F/cm^2$ and a synaptic radius of 500nm, a minimal amount of ≈ 4000 sodium ions would be required to raise the potential of about 20mV. Due to the overlap of sodium entry and potassium exit (during action potential), we consider that 4 times more ions are required[10]. With a published conductance of 750fS for ChR2-XXL[5], a single channel would conduct 300000 ions/s at such an electrochemical driving force, taking about 100ms to depolarize the synaptic compartment sufficiently. Because we are using an ultrasensitive ChR, called ChR2-HRDC, with an improved conductance and membrane stability, in principle we would only need one active

channel to produce a depolarization of ≈20mV to elicit secondary responses critical for signal propagation.

We were next interested in the photon density at increasing distances to the emitting presynaptic compartment. We thus performed Monte Carlo simulations of photon propagation through homogeneous biological, to assess the effect of light scattering and absorption with different wavelengths of emitted light. To do so, we considered a point emitter of the size of the synapse (r=500nm), in the same order of magnitude as the emitted light, emitting light isotropically in all dimensions. We simulated three different scenarios, considering the different luciferases exploited in this work with $\lambda_1 = 475$nm for Turquoise-eNL (TeNL), $\lambda_1 = 515$nm for the mNG-eNL (GeNL) and $\lambda_1 = 600$nm for the CaMBI luciferase (Extended Data Fig. 8). We implemented a formal probabilistic solution for the equation of radiative transfer through turbid media in the framework of biological tissues in order to provide an estimate of the quantity of light that is received by a postsynapse at distance d when emitted by a point source. Importantly, the light received by the postynapse at a distance d decreases with the opening angle θ of the steradian, that embraces the plane of the synapse (Supplementary Fig. 8), independent of scattering and absorption. This geometric factor is equivalent to a dilution of finite number of photons, similar to chemicals in a bulk. In any turbid medium, including biological tissue, photons undergo reflection, refraction, scattering and absorption, that changes the probability of finding a photon along the direction of propagation. To simulate the scattering and absorption of photons in the tissue, we implemented a random walk using a Metropolis Hastings algorithm which is a Markov chain Monte Carlo method (MCMC, details can be found in Ref. [11,12]). The two combined effects, photon dilution and absorption lead to a rapidly decreasing photon density with increasing detector-source separation. More quantitatively, considering our photon budget from above, from the $4.5{\cdot}10^6$ photons available, only ≈100 photons pass through a point at a distance of 1 mm, the length scale of the worm (Supplementary Fig. 9). In other words, the likelyhood of activating the ChR-HRDC at

a distance 1mm away from the synapse decreases 10.000 fold.

The parameters we used for the scattering simulation were for 480 nm $\mu_a = 0.6cm^-1$, $\mu_s = 120cm^-1$, $g = 0.88$, $n = 1.4$ and for 600nm $\mu_a = 0.15cm^-1$, $\mu_s = 90cm^-1$, $g = 0.86$, $n = 1.4$ where they correspond to the absorption coefficient, scattering coefficient, anisotropy factor and refraction index respectively [13]. The absorption coefficient can be represented as the sum of the contributions from all absorbing chromophores in the tissue [14]. Therefore, we summed the blood absorption contribution adopting the convention followed by Ref. [14]

$$\mu_{a.blood} = \frac{\epsilon ln(10) C_{mHGb}}{MW} = 0.0536\epsilon_{blood}$$

where ϵ_{blood} is the extinction coefficient which varies with the wavelength. To perform this calculation, we used the values given in [14].

Choice of the Luciferase and the Channelrhodopsin We reasoned that the spectral overlap between the luciferase emission and ChR2 absorption is critical for the function of the system and thus we only considered a combination of TeNL with blue-activated ChR2 and mNeonGreen fused eNL in combination with ACR1. Given the estimated resting Ca^{2+} concentration of 60-90 nM in ASH[15], we chose a calcium sensor domain with a K_d of 250 nM in order to maximize the sensitivity and dynamic range of our TeNL[2]. However, using red-shifted ChR2 like Chrimson or ChRmine[16], we anticipate that luciferases like CaMBI are superior[17]. Even though the common firefly luciferase emits photons that peak at Chrimson absorption, we were unable to observe a large photon production in transgenic animals for firefly luciferase.

We first considered the general ChR2-H134R as photosensitizer, but discarded it due to the low operational light sensitivity and its inability to drive a behavioral response with PhAST. We then turned our attention to the high photocurrent ChR2 bearing the mutation C128S;L132C;H134R[18]

(hereafter termed ChR2-triple) and generated transgenic animals expressing ChR2-triple in AVA (Supplementary Fig. 10a). In young adult animals, we observed a strong response at 2.4mW/mm^2, but a fast habituation to repetitive stimuli (Supplementary Fig. 10). Moreover, older (day 2 onwards), animals lost their ability to respond to blue light, due to neuronal degeneration, visible as loss of AVA (Supplementary Fig. 10a, c). We suspected that a continuous depolarization in presence of ATR led to this effect. We thus generated the double mutant ChR2-HRDC[18], which we employed in this study for downstream experiments due to its ability to repetitively drive behavior in *C. elegans* at extreme low light intensities. We also tested the red-shifted ChRmine, an unconventional pump-like channelrhodopsin maximally responding to orange light, but could not match the same operational light-sensitivity as with the cyan-activated ChR-HRDC (Fig. 2).

2 Supplementary Text 2: CRE recombinase expression

In a first attempt to overlap expression of *eat-4* and the CRE recombinase, we used the *octr-1* promoter, which was described to be expressed in a restricted number of cells in the head [19]. After confirming a restricted expression and overlap with ASH (Supplementary Fig. 11a) of the *octr-1* promoter cloned, we tested the response to nose touch of worms coexpressing the floxed *eat-4* allele and *octr-1p*::CRE. Animals failed to respond consistently to nose touch and frequently lost the mTagBFP2 marker in somatic tissue, displaying ubiquitous recombination pattern in all cells, which we attributed to the reported expression in spermatheca and/or germ line.

To avoid the spurious recombination in the germline, we performed a split-CRE [20] approach in which we targeted the 3.8kB *sra-6* promoter [21] together with *gpa-13* promoter and the split form of CRE (Supplementary Fig. 11b). We observed successful reconstitution of the CRE activity in 2-4 cells in 90% of the animals, which correlated with a decrease in nose touch response in animals coexpressing the floxed *eat-4* allele (Supplementary Fig. 11b). This confirmed that *eat-4*

was effectively excised with the split CRE, without affecting other tissues.

We reasoned that splitting the CRE enzyme might result in a recombination efficiency $<100\%$. In order to increase the recombination efficiency in ASH, we surveyed various promoters that exclusively drive expression in glutamatergic neurons involved in nose touch. Since we also use a CRE/lox strategy to obtain AVA-specific ChR2 expression, we looked for promoters with an overlap on ASH and AVA. Recently, Schmitt et al [22] proposed an intersectional strategy using a *gpa-14p*::CRE and a *flp-18p* transgene that generates an AVA restricted transgene expression after recombination. Among other neurons in the head where *gpa-14* is expressed (Supplementary Fig. 11c), ASH is the only neuron involved in nose touch. We confirmed recombination in ASH with coexpression of an *sra-6p*::GCaMP transgene, that leads to overlap in red and green channel. We then assayed nose touch and found a significant decrease in the reversal rate, similar to the other transgenes tested and what was observed before for ASH ([23], Supplementary Fig. 11c). We attributed the residual nose touch response to other nociceptive avoidance neurons, e.g. FLP. Indeed, when we deleted *eat-4* in FLP using a *des-2p*::CRE construct, in addition to ASH, we found a strong reduction in the nose touch response (Mean=1.8$\pm$SD1.6, N=32 animals, p=0.0003 derived from two tailed, unpaired t-test).

3 Supplementary Text 3: VC disinhibits vm2 possibly through uv1 inhibition

The observation To dissect the egg laying circuit we expressed tetanus toxin either in the two motorneurons HSN and VC alone or in both classes together. In all three combinations, we observed a noticeable reduction in spontaneous calcium activity in vm2 vulval muscles, suggesting that these low amplitude flickers are at least in part due to synaptic input from their motorneurons. The defect of the calcium flickers due to HSN::TeTx could be rescued when we express PhAST in HSN, but we could not rescue the calcium transients when VC neurotransmission was perturbed

after TeTx expression. We thus asked, how do VC neurons that express TeTx inhibit vm2 calcium activity without synaptic transmission? VC neurons have recently been proposed to have a direct inhibitory effect on HSN through metabotropic cholinergic receptors *gar-2*[24,25]. We reasoned that direct inhibition of HSN or vm2 cells [24,25] should be absent in VC::TeTx animals that lack synaptic output. Therefore, we propose an additional, indirect but dis-inhibitory role of VC on calcium activity in vm2, through neuroendocrine uv1 cells as candidates (Supplementary Fig. 12). These specialized, neuron-like cells are known to negatively modulate HSN, but also vm2 activity through tyramine[26] and neuropeptides[27]. Our results suggest that without inhibition from VC, uv1 might constitutively suppress either vm2 calcium signaling or HSN activity.

The model In order to visualize the impact of such disinhibitory connections on overall vm2 calcium dynamics, we set up a computational circuit model based on the assumptions presented in [28], with the important difference that we model calcium activity and not egg-laying. Thus, our model does not rely in proprioceptive feedback and solely contains four nodes and four edges with different polarity connecting them. With this model, we simulate vm2 calcium activity, based on stochastic transitions over a barrier that separates the active/inactive state of each node. We consider three hypothetical scenarios, based different connectivity pattern between VC, uv1 and vm2 cells. Importantly, the model neither attempts to reproduce the temporal scales of egg-laying reported earlier[28], nor charateristic bursts-like patterns observed in the egg laying behavior.

Scenario 1: The model describes the states of 3 neurons VC, UV and HSN, and calcium dynamics in vm2

- **VC state:**

$$p_1 = p(vc_{t+1} = 1 | vc_t = 0) = \lambda_3, \tag{1}$$

where $\lambda_3 = 0.02sec^{-1}$.

$$p_2 = p(vc_{t+1} = 0 | vc_t = 1) = \lambda_1 \tag{2}$$

- **UV state:**

$$p_3 = p(uv_{t+1} = 1 | uv_t = 0) = \begin{cases} 1 & \text{if } vc_t = 0 \text{ or } vc_{\text{TeTx}} \\ 0 & \text{otherwise} \end{cases} \tag{3}$$

$$p_4 = p(uv_{t+1} = 0 | uv_t = 1) = \begin{cases} \lambda_2 & \text{if } vc_t = 0 \text{ or } vc_{\text{TeTx}} \\ 1 & \text{otherwise} \end{cases} \tag{4}$$

- **HSN state:**

$$p_5 = p(hsn_{t+1} = 1) = \begin{cases} \lambda_4 & \text{if } uv_t = 0 \\ 0 & \text{otherwise} \end{cases} \tag{5}$$

- **Ca^{2+} concentration in VM**

$$\frac{dx}{dt} = -x/\tau + I_{\text{Ca}} \tag{6}$$

$$I_{\text{Ca}} = I_{hsn} + I_{vc}, \qquad \text{with} \tag{7}$$

$$I_{hsn} = \begin{cases} \lambda_5 & \text{if } hsn_t = 1 \text{ and not } hsn_{\text{TeTx}} \\ 0 & \text{otherwise} \end{cases} \tag{8}$$

$$I_{vc} = \begin{cases} 0.1\lambda_5 & \text{if } vc_t = 1 \text{ and not } vc_{\text{TeTx}} \\ 0 & \text{otherwise,} \end{cases} \tag{9}$$

The time constants λ_1 and λ_2 corresponds to intervals induced by vc and uv1 respectively, and were proposed in original model, $\lambda_1 = \frac{1}{23} sec^{-1}$ and $\lambda_2 = \frac{1}{1800} sec^{-1}$ [28]. The time constant $\lambda_4 = 0.05 sec^{-1}$ was selected to reproduce the approximate frequency of calcium events. $\lambda_5 = 0.2$ has an arbitrary units to reproduce the calcium dynamics. τ corresponds to the time-scale of calcium efflux from VM, and was set to $1sec$. This model does not take into account direct inhibition of HSN by VC which was proposed by ref. [25]. After simulating the spontaneous calcium dynamics in vm2, we found a surprisingly similar pattern (Supplementary Fig. 12) compared with experimentally derived kymographs.

Possible molecular pathway and alternatives VC neurons do not form synapses with uv1 cells[29]. We thus hypothesize a neuromodulatory role of acetylcholine secreted from VC neurons on the primarily inhibitory neuroendocrine uv1 cells. These cells strongly co-express all three metabotropic acetylcholine receptors GAR-1,2,3 and their $G_{i,o}$ effector G-proteins[30]. Thus, silencing VC neurotransmission does not only remove the direct synaptic excitatory effect on vms, but might also remove the indirect disinhibitory effect through uv1. We also considered an inhibition of vm2 directly from uv1 without gross changes in simulation outcome. Interestingly, vm2 also strongly express metabotropic acetylcholine receptors and inhibitory $GG_{i,o}$ proteins in addition to SER-2, the tyraminergic receptors. Overexpression of *ser-2* causes mild egg-laying defects, coinciding with their weak expression in vm2[30]. This provides an alternative plausible inhibitory connection from uv1 to vm2. However, because the calcium dynamics in the vm2 cells after PhAST reconstitution are considerably faster that the gating dynamics of the ChR2-HRDC, the effect of the PhAST might be to sensitize vm2 cells to ongoing synaptic input. Thus, PhAST might cause subthreshold depolarization that transiently enhanced action potential activity due to external input. We would like to stress though, that the measured spike time intervals are estimated from the fit of the deconvolution algorithm[31] to the calcium recordings and do not necessarily de-

scribe the interval between two consecutive calcium transients. Rather, many fast repetitive spike intervals are convolved by the long lasting calcium events (see also Supplementary Fig. 7). Taken together, using PhAST, we deciphered how HSN and VC transmission at the neuromuscular junction influence vulval muscle calcium activity and found a previously unrecognized role of VC motor neurons, possibly through metabotropic signaling on uv1 cells to disinhibit muscle calcium activity.

4 Supplementary Text 4: Towards universal expression tools

Strain/plasmid	**Tissue**	**Tool**	**System**	Addgene ID
MSB966	muscles	ChR2-HRDC	CRE/lox	n/a
MSB1160	neurons	ChR2-HRDC	CRE/lox	n/a
MSB1232	neurons	ChR2-HRDC	CRE/lox	n/a
MSB952	any	ACR1	UAS	n/a
MSB964	pan-neuron	ChR2-HRDC	CRE/lox	n/a
MSB985	neurons	ChRmine	CRE/lox	n/a
MSB961	neurons	ACR1	CRE/lox	n/a
pNMSB139	systemic	ChR2-HRDC	CRE/lox	199312
pNMSB131	systemic	ChR2-HRDC	CRE/lox	199311
pNSMB88	any	Teal-Nanolantern	UAS	199321
pNSMB109	any	CaMBI	UAS	199322
pNMSB91	any	ACR1	UAS	199319
pNMSB97	pan-neuron	ChR2-HRDC	CRE/lox	199317
pNMSB96	flp-18p	ACR1	CRE/lox	199316
pNMSB104	flp-18p	ChRmine	CRE/lox	199314
pNMSB132	pan-neuron	ChR2-HRDC	CRE/lox	199310
pNMSB84	flp-18p	ChR2-HRDC	CRE/lox	199309
pNMSB99	muscle	ChR2-HRDC	CRE/lox	199308

In order to facilitate usage of the engineered constructs and tools, we have established several effector cassettes for bipartite expression systems, such as UAS/Gal4 and Cre/lox transgenic animals. These effector strains can then easily be crossed together with driver strains and or injected directly with the driver construct to obtain single cell or single tissue expression. The inventory of

PhAST tools that can be directed using bipartite expression systems is shown in the table below. Details about genotype and expression cassette can be found in Supplementary Table 4.

5 Supplementary Text 5: Protocols and Reagents

Molecular Biology

Expression of light-gated channels and jRGECO1a in AVA We used an intersectional strategy for cell-specific expression in AVA[22]. We first generated a lox2272-mTagBFP2-stop-lox2272::ChR2Triple-SL2-jRGECO1a construct in a universal MosSCI plasmid[32] by synthesising and assembling mTagBFP2(sequence from pJJR81, Addgene plasmid #75029)::*tbb-2* 3'UTR, ChR2Triple [18] and SL2::jRGECO1a fragments downstream *flp-18p*. Co-expression with *gpa-14p*::CRE, directed ChR2 expression only in AVA. Conversion of ChR2-Triple to ChR2-HRDC was carried out through a CRISPR reaction (Supplementary Table 3). All reagents purchased from IDT and conditions for injection were: 12.5 μM each crRNA, 2 μM crRNA for *dpy-10*, 27 μM tracrRNA, 6 μM Cas9, 0.5 nM *dpy-10* ssODN and 1.75 nM homology repair template. ACR1 expression was accomplished by replacing ChR2-HRDC in pNMSB84 by the ACR1 ORF, was amplified from the transgenic strain ZX2024 [18]. To express ChRmine in AVA, we generated pNMSB104 by replacing ChR2-HRDC in pNMSB84 with ChRmine.

Expression of light-gated channels and jRGECO1a in AIB pNMSB34 was constructed with the sequence for *npr-9* promoter described in [33]. pNMSB37 was constructed inserting YFP from pSX317 (gift from Shawn Xu, [6]) between ChR2-HRDC and SL2::jRGECO1a by Gibson assembly. pNMSB105 was constructed by amplifying *npr-9* promoter from pNMSB34 and inserting it into pNMSB96 in front of ACR1. pNMSB113 was constructed by replacing ChR2-HRDC in pNMSB34 with ChRmine::wrmScarlet.

Expression of light-gated channels and jRGECO1a in vm2 An intersectional strategy was used for cell specific expression in vm2. The universal MosSCI plasmid pNMSB99 was generated by replacing the *flp-18* promoter in pNMSB84 by the *myo-3* promoter from pCFJ104. Co-expression with *unc-103Ep*::CRE[34], restricted ChR2-HRDC in vm2s.

AVA::CRE For *gpa-14p*::CRE, pNP259 plasmid described in [22] was used.

vm2::CRE For *unc-103Ep*::CRE, primers described in [34] were used to amplify N2 genomic DNA and the resulting fragment cloned in front of CRE, generating pNMSB111.

ASH:CRE ***Split CRE*** [20] The N-terminal fragment of CRE (aa 1-244) was synthesized flanked by NaeI and EagI restriction sites and subsequently cloned into a vector containing a *gpa-13* promoter and *unc-54* 3'UTR (pNMSB5). The synthetic C-terminal fragment of the split CRE (aa 245-345) was flanked by SmaI and EcoRI restriction sites and cloned into pSX318 (gift from Shawn Xu, [6]) after the 3.8 kb *sra-6* promoter. The 2.0 kb *sra-6* promoter driving C-CRE expression in pNMSB45 was generated by directed mutagenesis with primers specified in Supplementary Table 2.

octr-1p*::CRE octr-1* promoter was amplified from genomic DNA (Supplementary Table 2) and cloned into pNMSB7 together with the two intron CRE::tbb-2 3'UTR in pDD282[35]. The fragment *octr-1p*::CRE::tbb-2 3'UTR was then moved to the universal MosSCI vector pNMSB28.

Expression of calcium sensitive, enhanced Nanolanterns and CaMBI TeNL was synthesized using a *C. elegans* codon optimized version of mTurquoise2 and the Ca^{2+} 250 eNL described in reference [2]. For ASH restricted expression (pNMSB16) the 2000 proximal bp of the *sra-6* promoter were used. pNMSB17 was constructed amplifying the *eat-4* promoter from genomic DNA and replacing the promoter in pNMSB16. pNMSB40 was built by replacing the mCherry driven by the *myo-3* promoter in pCFJ104 by TeNL. For AWA specific expression (pNMSB130),

the *odr-7p* promoter described in [36] was used in front of the TeNL. For expression in VC neurons (pNMSB89) the *lin-11* enhancer described in [24] was cloned in a plasmid containing delta *pes-10* minimal promoter driving TeNL. In HSN, expression of TeNL was achieved by replacing the *sra-6* promoter in pNMSB86 with the *egl-6a* promoter described in[37] (pNMSB125).

Green enhanced Nanolantern[2] (GeNL) was generated amplifying mNG from pDD268[35] and codon optimized CaMBI[17] (calcium affinity 300nM) was synthesized. Both were inserted into pNMSB86 replacing TeNL under the *sra-6p* promoter to generate pNMSB92 and pNMSB100 respectively.

Targeting TeNL to pre-synaptic regions in ASH To build pNMSB26, the sequence for *sng-1* was synthesized and introduced between the *sra-6* promoter and TeNL in pNMSB16 with a flexible linker between them.

ASH:jRGECO1a pNMSB72 was constructed by replacing in pNMSB6a the regions corresponding to *flp-18* promoter, mTagBFP2 and ChR2 by the 2.0 kb *sra-6* promoter and the miRFP670 ORF (addgene-plasmid-79987, see Supplementary Table 2).

Expression of Tetanus toxin light chain (TeTx) The sequence for the TeTx was codon optimized and synthesized. To drive expression in VC neurons, it was cloned into pNMSB89 with an SL2 after TeNL (generating pNMSB98). To generate pNMSB112, overlaping primers on pNMSB98 to remove the TeNL::SL2 fragment were used in a PCR reaction. To drive expression in HSN, *egl-6* promoter was introduced into pNMSB98, replacing *lin-11e::delta pes-10* promoter and generating pNMSB124.

Microfluidic device characterization

Finite Element Analysis (FEA) In real case, the hydrostatic pressure applied in the channel also deforms the sidewalls of the actuator. In order to have a prediction that is more accurate we performed numerical simulation based on FEA. Therefore we considered the surrounding walls in the simulation. The actuator is simulated with Ansys workbench (2021 R1). The material is set as a PDMS block as obtained from a 1:15 mixing ratio cured at 85°C for two hours with the specification of Young's modulus of 1.4 MPa and 0.5 Poisson's ratio with tensile strength 2.24 MPa [38]. The model is meshed using structured hexahedral grids (Extended Data Fig. 2) to reduce the mesh size and thus computational cost while maintaining the appropriate grid quality. We conduct mesh independence studies in CFD (computational fluid dynamics) to make sure that the results we get are due to the boundary conditions and physics used, not the mesh resolution. Mesh independency is assessed based on total deformation. Average cell size is sequentially reduced until the displacement difference is independent from the grid size. The obtained results are independent of the mesh size above 127320 nodes. Thus, the cell size corresponding to the case with 127320 nodes is chosen for the numerical investigation. The actuator was studied under three pressure rates (0, 150, and 350 kPa). Both results from the Eq. 1 (as described in the methods) and simulation showed that lower thickness results in steeper slope, which requires lower pressure to apply in the channel to achieve the desire deflection. To optimize the dimensions of the actuator, different width, thickness and height were studied. Since the channel geometry is set by the dimensions of the animals and cannot be changed, thickness and elasticity of the diaphragm are the major design variables permitted. Lower thickness plays an important role to increase the deflection but lower than 10 microns is challenging from fabrication point of view. Measurements confirmed that the length of the channel had a negligible effect on membrane deflection.

Egg laying behavior

Optogenetics Late L4-YA animals were cultivated overnight in the dark at 20°C on NGM with OP50 with or without all-trans retinal (ATR)[39,40] at 0.1 mM final concentration. 16h later, animals were transferred to a 35 mm plate without food and imaged over a comertially purchased LED array, designed in [41]. Animals were illuminated for 30 seconds with white light (5 μW/mm^2) and then 477 nm blue light at 9 mW/mm^2 was shone on them for 30 seconds more. Light output was controlled by a Neopixel panel controller and software prepared for the experiment in Arduino IDE. Videos were collected using Imaging Source DMK38UX255 camera and IC Capture software. Each worm laying eggs was scored as a positive event. Three experimental replicates were performed.

Calcium imaging of vulval muscles L4 worms were cultivated overnight in the dark at 20°C on NGM and OP50 with or without all-trans retinal (ATR)[39,40]. The FFz solution was prepared by mixing 3μL of FFz (stock concentration 20 mM) with 15μL of 5x OP50 bacterial solution (with and without ATR) and worms were transferred to the FFz/OP50 solution and incubated at RT without light for 30 minutes before imaging. Image was performed on 6% agar pads and 5-10μL of microsphere beads (Polybead® Microspheres 0.10µm, Polyscience, Cat no. 00876-15) to immobilize animals. The calcium signal was recorded using a Leica DMi8 inverted optical microscope. The jRGECO1a signal was excited with a 555 nm beam (intensity =10%) at 85 ms exposure time and the emitted wavelength was filtered using a @595/31 Brightline HC filter. A 40x/1.1 - water WD 0.65mm objective lens was used with the 512 x 512-pixel field of view. The fluorescent signal was detected with a Hamamatsu Orca Flash 4.3 and the LED laser power was controlled by Lumencore software. The calcium imaging was conducted using HCImage software to record 40-sec videos of vm2::jRGECO1a saved as MPTIFF format.

Calcium analysis The jRGECO1a intensity was extracted from the vm2 regions in the raw image stacks in ImageJ, binned and processed with the percentile method as described above for neurons. The non-stationary baselines were corrected in R with the `baseline` package (see below) after smoothing individual traces with a 5-frame moving average to remove hot pixels and spurious outliers. To detect and quantify the peaks in the noisy data, we used the L0-penalized method and employed a model that connects the observed fluorescence information to the underlying and unobserved calcium concentration and 'firing' time[42]. The model uses two hyperparameters, $\gamma = 0.95$ and $\lambda = 0.05$, which were maintained constant for all conditions. Due to the lack of ground truth spike data, training of the model was not possible and the hyperparameters were determined as follows: γ was chosen according to [43] $1 - \frac{\Delta}{\phi}$, with Δ as the parameter characterized by the framerate f of the camera $(1/f)$ and $\phi = 2$ characterizing the speed of the calcium dye. We determined λ empirically based on the firing rate, decay rate, and estimated signal-to-noise ratio and choose the best matching parameter that minimized the residuals $(r_M - r_D)$ between the model output and actual input dataset (Supplementary Fig. 7, [44]). Because many curves do not visually show a calcium signaling event, we allowed for zero value outputs. To avoid under-representation of these curves with low frequencies, we counted them as a single event with t_{spike}=60s. Spike times and intensities were tested against each other in a pairwise KS-test and the null hypothesis was rejected at the level of significance α=0.01.

Confocal microscopy

Fluorescence images were taken using an inverted research microscope (Nikon Eclipse Ti2) equipped with a spinning disk confocal microscope (Andor DragonFly 502, Oxford Instruments) on top of an active isolation table (Newport). A 60x/1.2 NA CFI Plan Apo VC water immersion objective and Andor Sona camera were used. mTagBFP2 was excited using the 405 nm laser, 30% power intensity and transmitted through a 445/46 nm emission filter. Exposure time varied between 30-100

ms, depending on the strain. mTurquoise2 was excited using the 445 nm laser, 30% power intensity and transmitted through a 478/37 nm emission filter. Exposure time varied between 100-200 ms. YFP was excited using the 514 nm laser, 20% power intensity and transmitted through a 552/41 nm emission filter. Exposure time was 30 ms. jRGECO1a was excited with 488 and 561 nm lasers, 30% power intensity each and transmitted through a 594/43 nm emission filter. Exposure time varied between 100-200 ms. mCherry was excited with a 561 nm laser, 10% power intensity and transmitted through a 647/63 nm emission filter. Exposure time was 30-100 ms. GCaMP/GCaMP7 were excited with a 488 nm laser, 40-80% power intensity respectively and transmitted through a 521/38 nm emission filter. Exposure time was 30 and 200 ms respectively.

6 Supplementary Figures

Supplementary Fig. 1

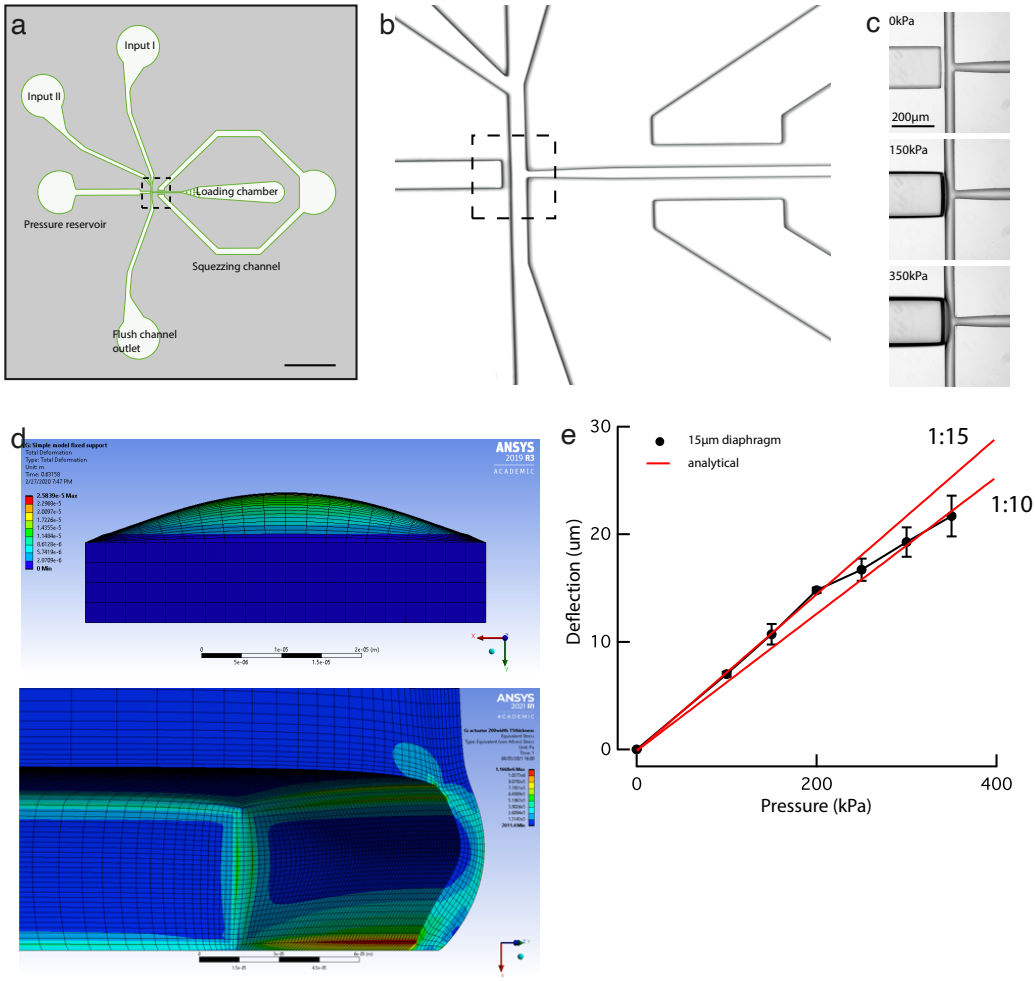

Design and calibration of the Trap'N'Slap design

a Layout of the microfluidic design. Scale bar = 1mm. **b** Photograph of the PDMS device of the dotted area shown in (a). **c** Photographs of the diaphragm deflection with increasing pressure on the channel of the dotted area shown in (b). **d** Finite element simulation of the plate deflection (top panel) showing the parasitic deformation of the bulk PDMS during the deflection. The bottom panel shows the stress contour in the device after inflation. **e** Measurement of the 15μm thick diaphragm deflection with increasing back pressure and the comparison to an analytical plate deflection model for two different PDMS mixing ratios 1:10 and 1:15 (red). Mean$\pm$SD, N=4 different diaphragms.

Supplementary Fig. 2

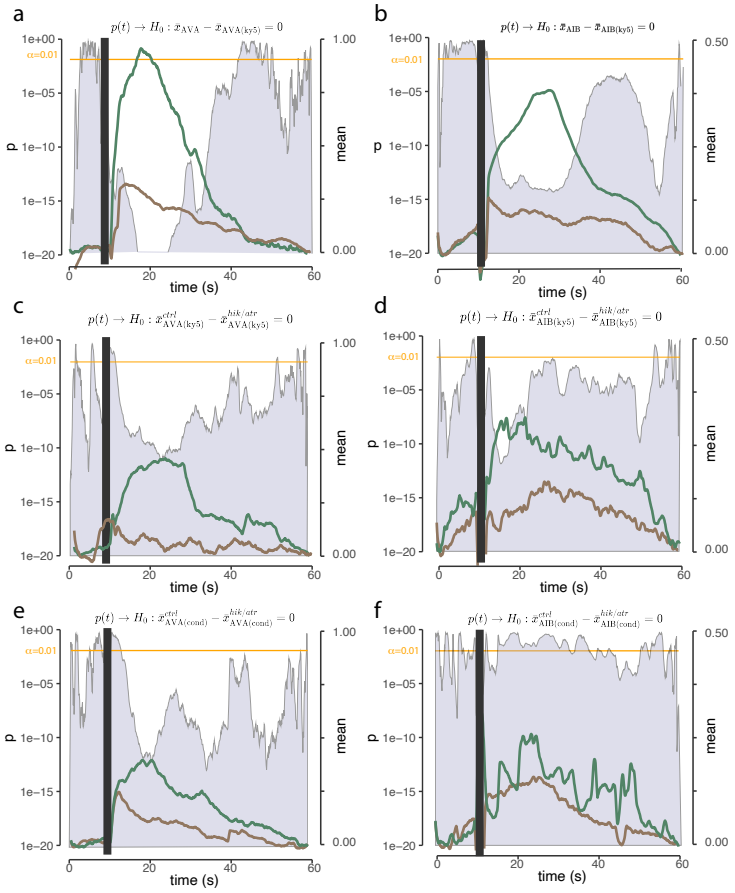

Statistical comparison of calcium recordings in AVA and AIB Plots showing the one-sided p-value (left axis) derived from a t-test statistics and the average calcium dynamics (right axis) vs time (bottom) for the indicated comparisons. The running, time-dependent *p*-value is indicated as shaded distribution, the alpha-level of significance indicated as orange line and the calcium dynamics of the tested measurements in green and brown. **a** jRGECO1a fluorescence in AVA in wild type vs in *eat-4(ky5)* animals. **b** jRGECO1a fluorescence in AIB wild type vs in *eat-4(ky5)* animals. **c** jRGECO1a fluorescence in AVA of *eat-4(ky5)* mutants vs AVA of *eat-4(ky5)* mutant animals treated with ATR+HIK. **d** jRGECO1a fluorescence in AIB of *eat-4(ky5)* mutants vs AIB of *eat-4(ky5)* mutant animals treated with ATR+HIK. **e** jRGECO1a fluorescence in AVA of *eat-4*(ASH) conditional mutants vs AVA of *eat-4*(ASH) conditional mutant animals treated with ATR+HIK. **f** jRGECO1a fluorescence in AIB of *eat-4*(ASH) conditional mutants vs AIB of *eat-4*(ASH) conditional mutant animals treated with ATR+HIK.

Supplementary Fig. 3

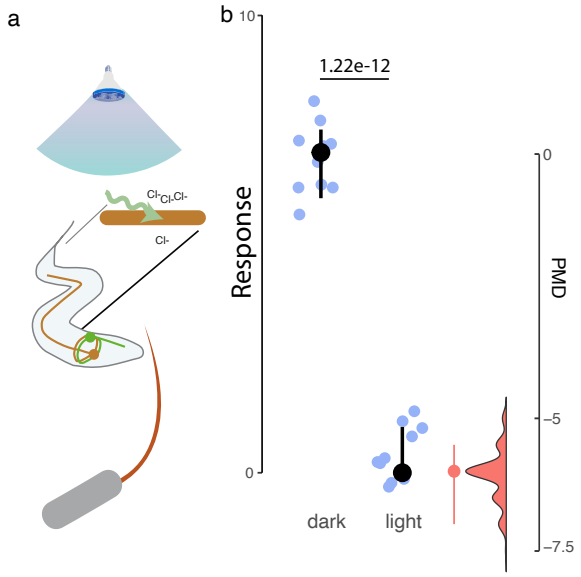

ACR1 suppresses nose touch response under external light a Schematic of the experiment. An animal is exposed to green light while ask to recognize an obstacle. **b** Quantification of the nose touch response of animals expressing ACR1 in AVA and AIB in the dark and under light after feeding with ATR. Only for display purposes, a scatter of 10% was applied to each datapoint to avoid overlap. Black circle indicates median, vertical bar indicates 95% confidence interval on the median. Floating axis indicates the paired median difference (PMD), derived from bootstrapping 100 independent distributions from the experimental data set. Red point indicates median, red vertical bar indicates 95% CI. Overlap of the CI with zero indicates low effect size and likely statistically insignificant distributions. Numbers on grey brackets indicate the two-sided *p*-value derived from a Wald-test.

Supplementary Fig. 4

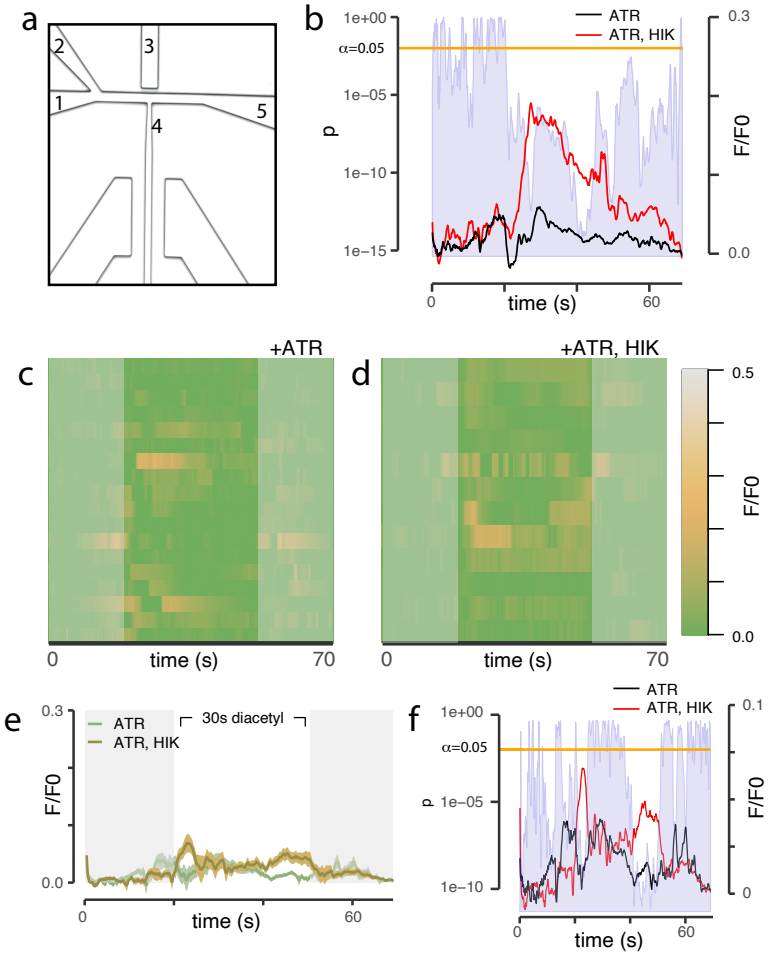

Calcium imaging in AVA and AIB in response to diacetyl

a Design of the combined olfactory and nose-mechanosensory chip (same as Extended Data Fig 2). 1) channel inlet for baseline buffer, 2) channel inlet for stimulation solution, 3) mechanical stimulation, 4) animal trapping channel, 5) buffer outlet. **b** one-sided *p*-value (without correction, left axis) derived from a t-test for the AVA calcium imaging experiments displayed in figure 5c (ii), comparing ATR-treated animals with ATR+HIK treated animals, indicated as shaded distribution, the alpha-level of significance indicated as orange line and the calcium dynamics of the tested measurements in black and red. **c-f** Calcium imaging in AIB in response to DA. c) Stacked kymographs of individual calcium recordings from animals treated with ATR (N=18) and d) with ATR+HIK (N=12). e) Average calcium response in AIB for conditions in c and d; and f) one-sided p-value (without correction, left axis) derived from a t-test comparing the two conditions, indicated as shaded distribution, the alpha-level of significance indicated as orange line and the calcium dynamics of the tested measurements in red and black.

Supplementary Fig. 5

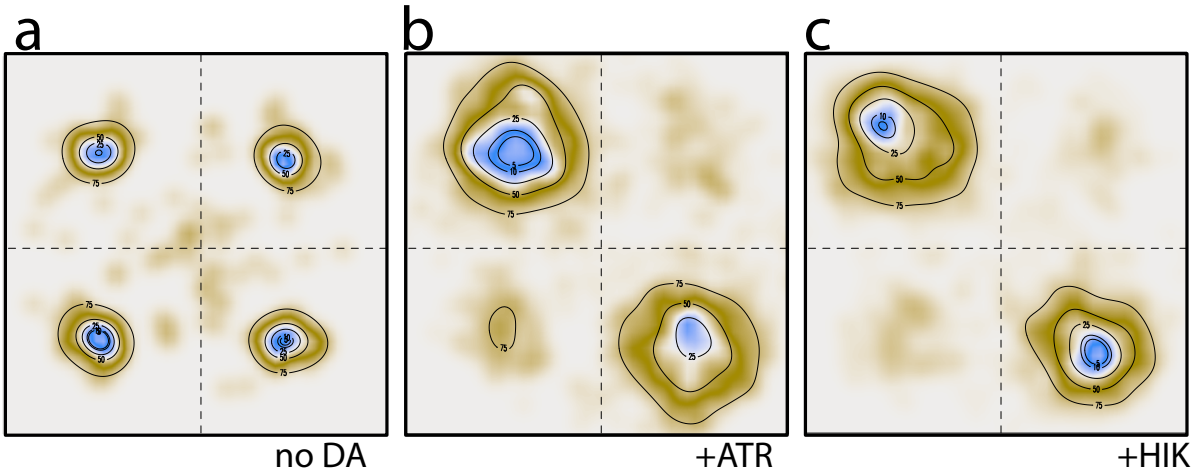

d

	vehicle	vehicle	vehicle	DA	vehicle	DA
# worms	117	109	165	1864	1400	1582
Condition	no atractant		control		control	
Strain	wild type				*odr-7(ky4)*	

	vehicle	DA	vehicle	DA	vehicle	DA	vehicle	DA
# worms	225	1633	159	1317	158	1002	244	874
Condition	control		HIK		ATR		HIK+ATR	
Strain	*AWA::TeNL, AVA::ChR2-HRDC, AIB::ChR2-HRDC*							

Chemotaxis experiment, controls a-c 2D-probability distribution of the chemotaxis assay in absence of diacetyl attractant (a), and in presence of DA with animals either cultured in presence of (b) ATR or (c) HIK. **d** Table with number of animals attracted or repelled by DA for all conditions.

Supplementary Fig. 6

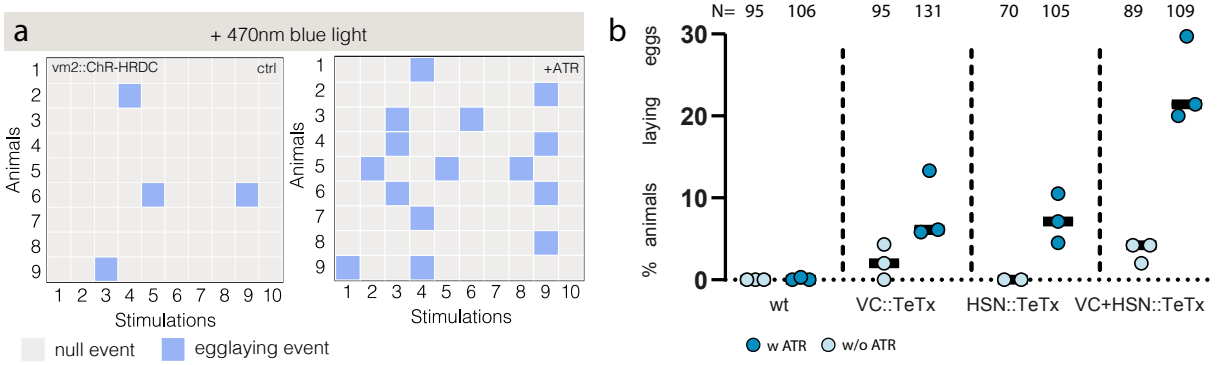

Egg laying response to blue light simulation a Raster diagram of egg laying events (blue squares) secondary to a 60s light stimulus in animals expressing tetanus toxin in VC and Channelrhodopsin in vm2 reared in absence and presence of ATR. **b** Percentage of animals that laid an egg after 30s of blue light stimulation in presence and absence of ATR. N=total number of animals assayed, for three independently replicated experiments. Thick horizontal line represents the median. Note, number of eggs laid increases in tetanus toxin expressing animals as they accumulate in their uterus.

Supplementary Fig. 7

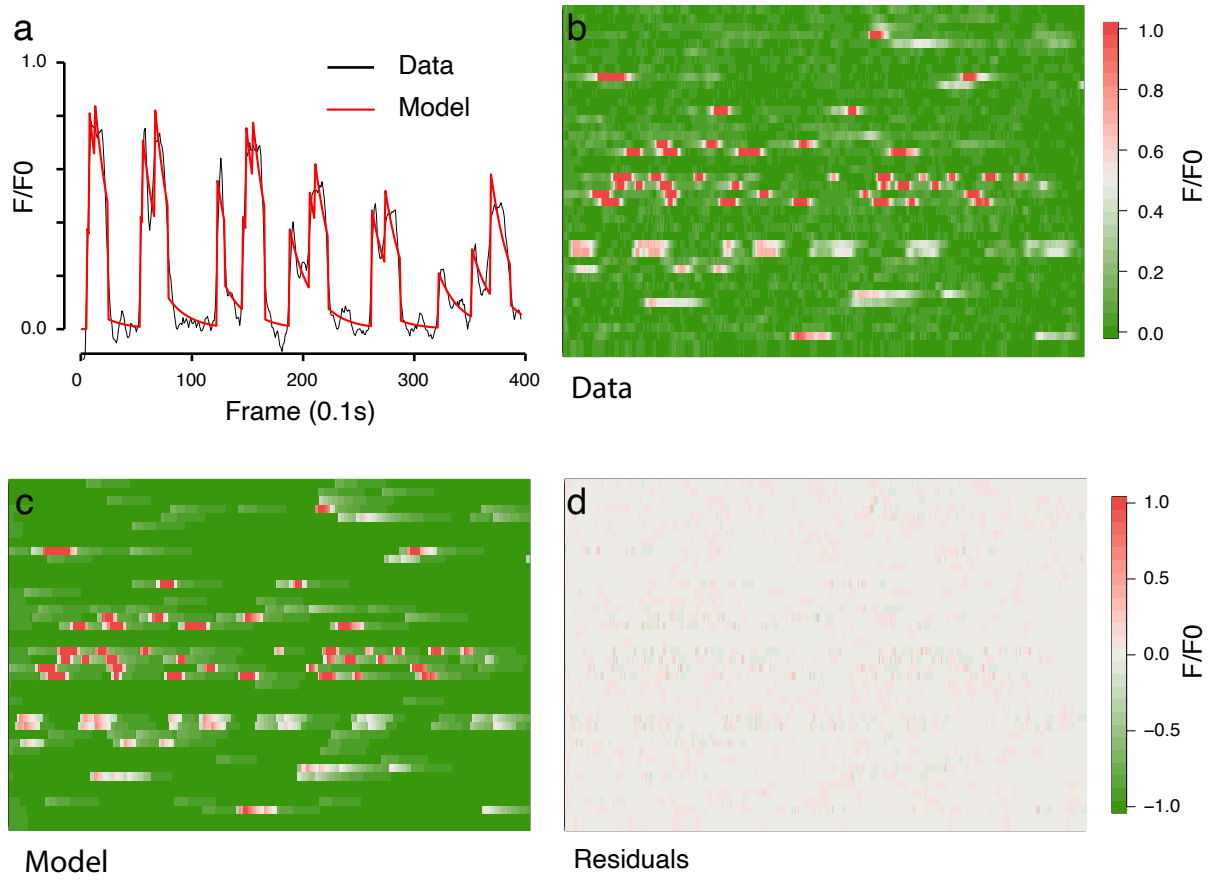

Modeling calcium fluctuations in vm2 a, Representative calcium trace (black) after baseline correction and the corresponding fit (red). Parameters were estimated as described in the Methods. Note, for each calcium transient, multiple spikes are estimated. **b, c,** Stacked kymographs of the (b) raw data and the (c) model output. Same data as in Figure 6e (i). **d,** Kymograph of the computed residuals between the raw data and the model fit.

Supplementary Fig. 8

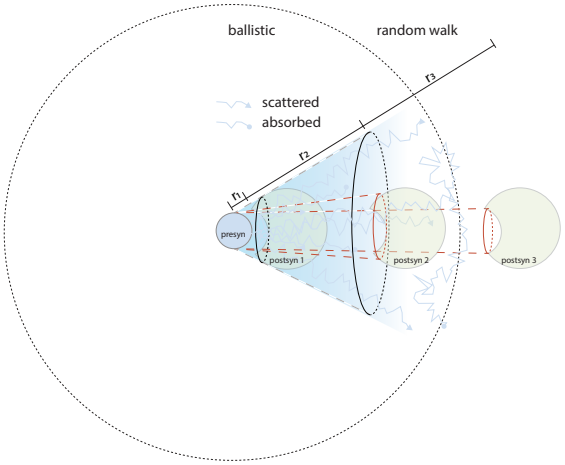

Hypothetical scenario for photon propagation in the vicinity of the synapse At close distances to the presynaptic compartment ($r << \lambda$), photons are not scattered or absorbed. With increasing distance, the probability of absorption and scattering increases, leading to an effective decrease in emitted light.

Supplementary Fig. 9

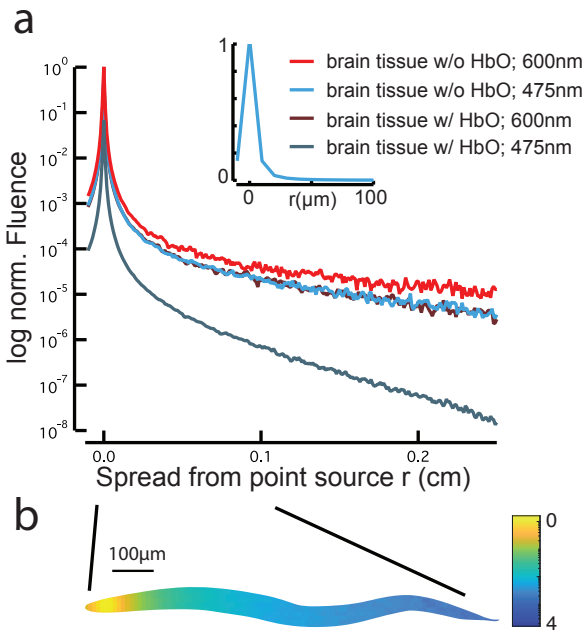

Photon propagation in living tissues a Monte Carlo simulation of photon propagation of 480 and 600nm wavelength. The plot shows the normalized log(Fluence) vs distance over the range of a living *C. elegans* animal. False-colored fluence in the worm indicates the point emitter as a neuronal synapse in the head. The inset shows the linear scale. Two scenarios were simulated with parameters described in the Supplementary Text 5, involving biological tissue without blood vessels and with absorption and scattering coefficients derived from brain tissue with oxygenated hemoglobin. **b** False colored heat map showing the calculated photon density with respect to the size and location of the worm. Emission was centered on ASH. Color scale is log transformed.

Supplementary Fig. 10

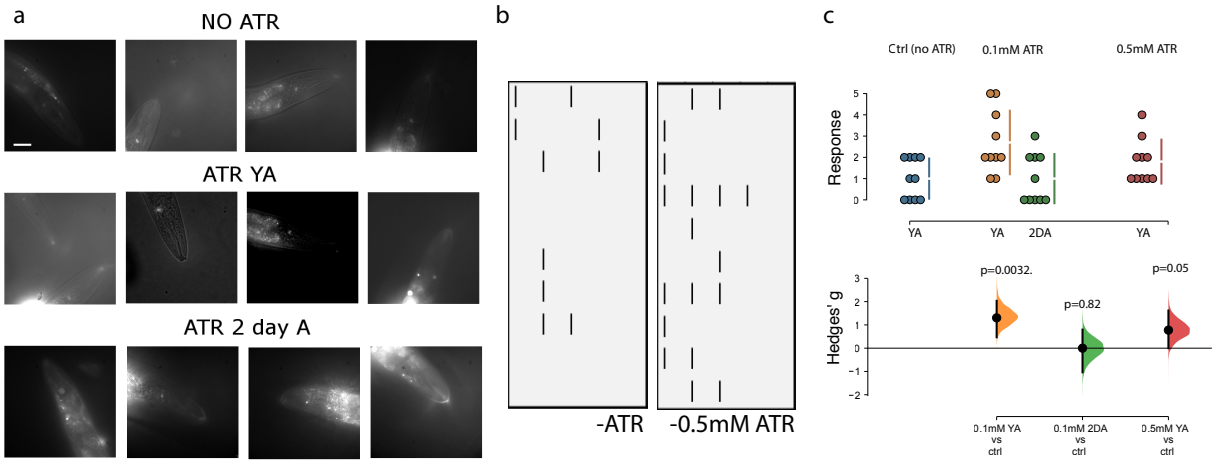

Expression of ChR2-Triple causes neurodegeneration in AVA a Representative pictures of young adult animals reared in absence of ATR, in presence of ATR and old animals in presence of ATR. **b,** Rasterplot of 10 animals stimulated five times with blue light cultured in absence and presence of ATR. **c,** Summary of the experiment with two different concentrations of ATR for N=10 animals. The Hedges' g for 3 comparisons against the shared control (no ATR supplementation) are shown in the above Cumming estimation plot. The raw data is plotted on the upper axes and represents the average response of 5 illuminations. Vertical bars indicate mean $\pm$ SD. On the lower axes, mean differences are plotted as bootstrap sampling distributions. Each mean difference is depicted as a dot. Each 95% confidence interval is indicated by the ends of the vertical error bars. The *p* value of the two-sided permutation t-test is indicated above the bootstrapped sampling distribution.

Supplementary Fig. 11

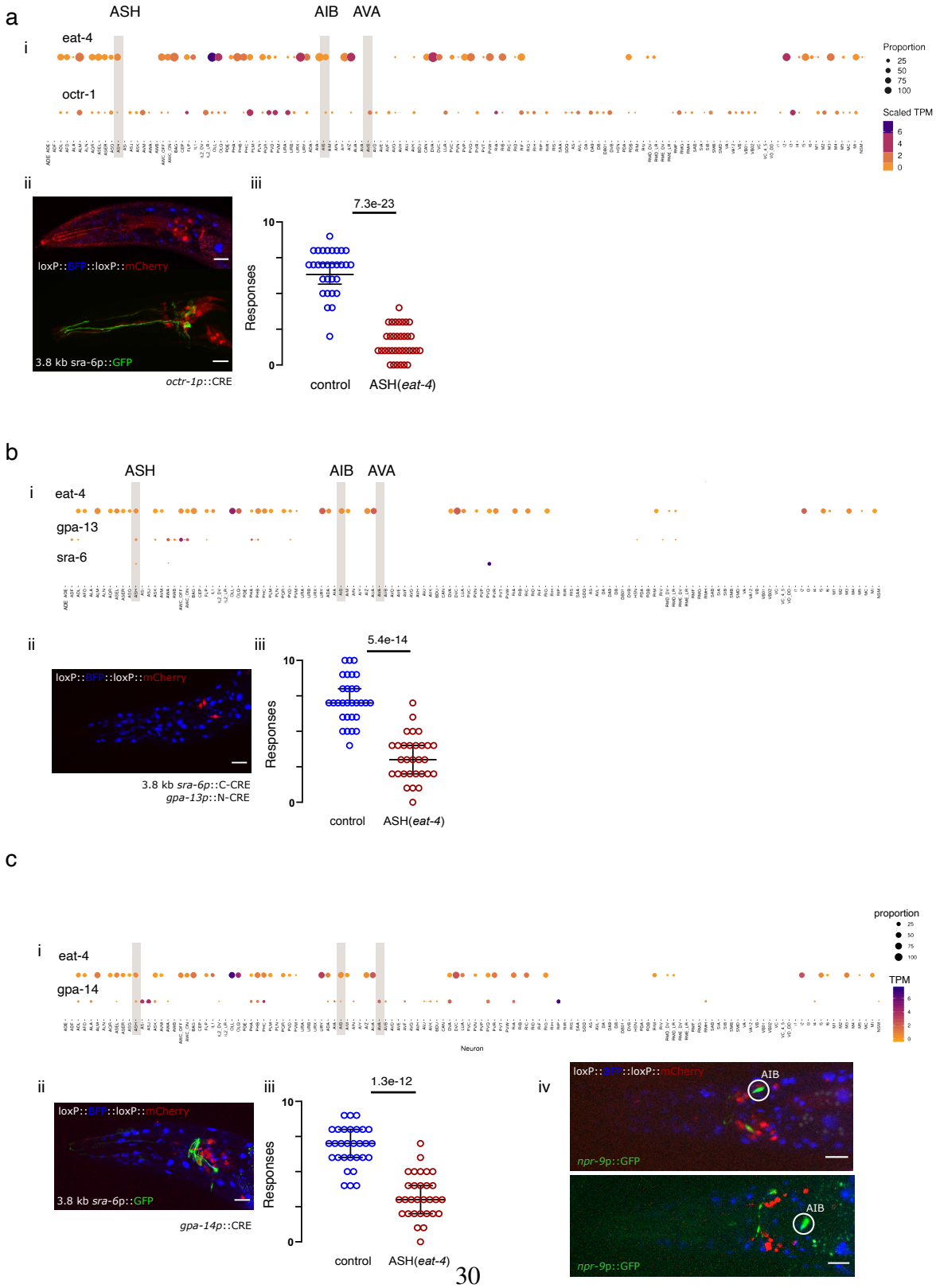

CRE expression under the control of different promoters. **a** Expression of CRE under the

control of the *octr-1* promoter. (i) Expression pattern of *eat-4* and *octr-1* as determined in [45] with overlap highlighted in ASH, AIB and AVA. (ii) Recombination was visible in ASH and two other cells as judged by coexpression with a *sra-6p*:GCaMP transgene known to drive in ASH [21] with the blue-red conversion. (iii) Nose response with the floxed *eat-4* allele and expression of *octr-1p*::CRE. **b** Expression of a split CRE to establish ASH-specific expression (see Methods). (i) Expression pattern of *eat-4*, *gpa-13* and *sra-6* as determined in [45] with overlap highlighted in ASH, AIB and AVA. (ii) CRE-loxP recombination pattern showing successful BFP>mCherry switch in cells in which the two promotors intersect and thus CRE is activity is reconstituted. (iii) Nose touch response of animals with a floxed *eat-4* allele and expression of the split *sra-6p*::C-CRE and *gpa-13p*::N-CRE. **c** Expression of CRE under the control of the *gpa-14* promoter. (i) Expression pattern of *eat-4* and *gpa-14* as determined in [45] with overlap highlighted in ASH, AIB and AVA. (ii) CRE-loxP recombination was tested in a color switch strain that expresses nuclear BFP in absence of CRE activity and nuclear mCherry in the cells where CRE is active. In addition, coexpression of mCherry with the ASH specific 3.8 kb *sra-6p* driving GFP expression was tested. (iii) Outcome of nose touch assays in worms with the floxed *eat-4* allele and expression of *gpa-14p*::CRE. p-value corresponding to an two tailed, unpaired, parametric t-test with 95% confidence interval. Median and 95% confidence interval are depicted in all dot plots. (iv) Representative images of a CRE-activity reporter animal expressing *gpa-14*p::CRE and *npr-9*p::GFP to highlight potential recombination in AIB. As can be seen by the absence of the GFP/mCherry overlap, *gpa-14*p::CRE does not drive recombination in AIB. Two different animals are representative for 8 randomly picked animals. Scale bars= 15 μm for all images.

Supplementary Fig. 12

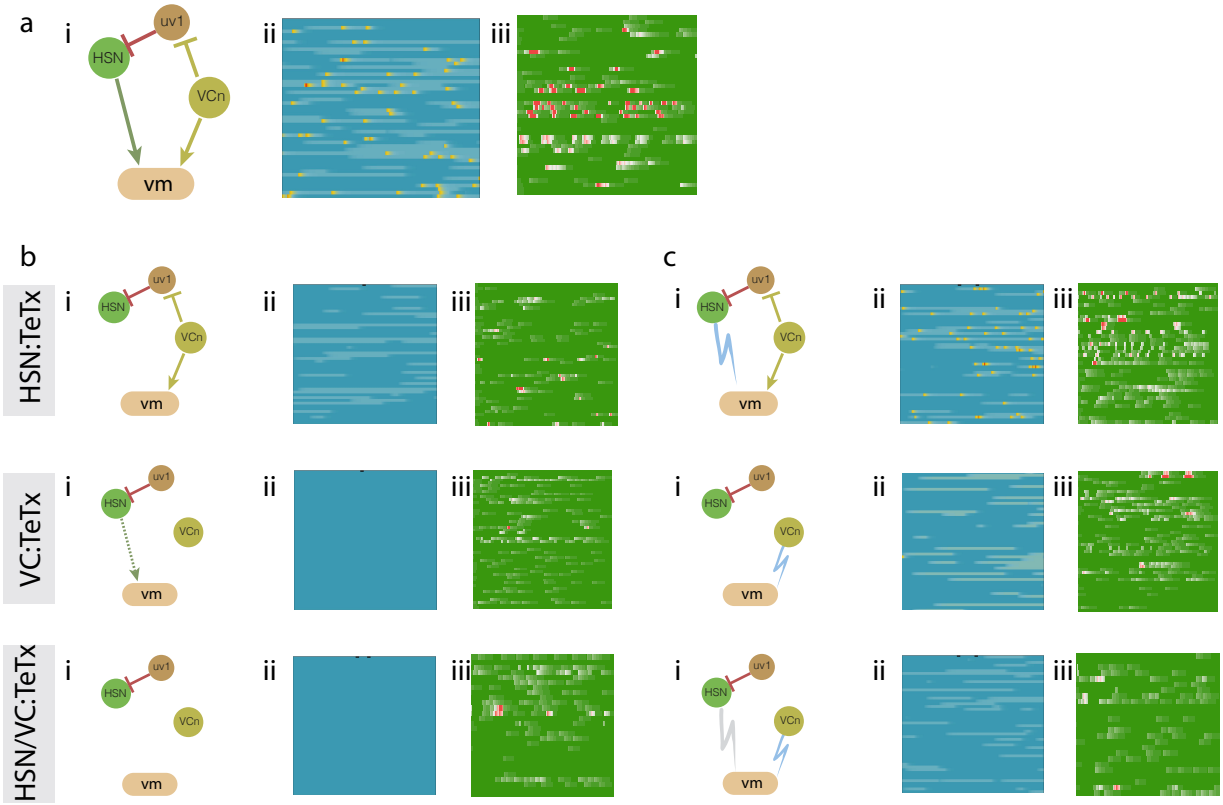

Simulations of the temporal patterns of vm2 calcium activity a-c Calcium activity of the untreated control animals, TeTx expressing experimental animals (b) without and (c) with functional PhAST components. i) Schematic of the egg-laying circuit incorporating a possible disinhibitory edge connecting VC and vm2 through the neuroendocrine cells uv1. ii) Simulated calcium activity and iii) experimental recordings of calcium activity.

Supplementary References

1. Lin, J. Y., A user's guide to channelrhodopsin variants: features, limitations and future developments. *Experimental physiology* **96**, 19–25 (2011).

2. Suzuki, K., et al., Five colour variants of bright luminescent protein for real-time multicolour bioimaging. *Nature Communications* **7**, 1–10 (2016).

3. Witvliet, D., et al., Connectomes across development reveal principles of brain maturation. *Nature* **596**, 257–261 (2021).

4. Hegemann, P., Möglich, A., Channelrhodopsin engineering and exploration of new optogenetic tools. *Nature Methods* **8**, 39–42 (2011).

5. Dawydow, a., et al., Channelrhodopsin-2-XXL, a powerful optogenetic tool for low-light applications. *Proceedings of the National Academy of Sciences* **111**, 13972–13977 (2014).

6. Piggott, B. J., Liu, J., Feng, Z., Wescott, S. A., Xu, X. S., The Neural Circuits and Synaptic Mechanisms Underlying Motor Initiation in C. elegans. *Cell* **147**, 922–933 (2011).

7. Mellem, J. E., Brockie, P. J., Madsen, D. M., Maricq, A. V., Action Potentials Contribute to Neuronal Signaling in C. elegans. *Nature neuroscience* **11**, 865–867 (2008).

8. Steger, K. A., Shtonda, B. B., Thacker, C., Snutch, T. P., Avery, L., The C. elegans T-type calcium channel CCA-1 boosts neuromuscular transmission. *Journal of Experimental Biology* **208**, 2191–2203 (2005).

9. Frøkjær-Jensen, C., et al., Effects of voltage-gated calcium channel subunit genes on calcium influx in cultured C. elegans mechanosensory neurons. *Journal of Neurobiology* **66**, 1125–1139 (2006).

10. Yu, Y., Hill, A. P., McCormick, D. A., Warm body temperature facilitates energy efficient cortical action potentials. *PLoS Computational Biology* **8** (2012).

11. Marti, D., Aasbjerg, R. N., Andersen, P. E., Hansen, A. K., MCmatlab: an open-source, user-friendly, MATLAB-integrated three-dimensional Monte Carlo light transport solver with heat diffusion and tissue damage. *Journal of Biomedical Optics* **23**, 1 (2018).

12. Periyasamy, V., Pramanik, M., Advances in Monte Carlo Simulation for Light Propagation in Tissue. *IEEE Reviews in Biomedical Engineering* **10**, 122–135 (2017).

13. Yaroslavsky, A. N., et al., Optical properties of selected native and coagulated human brain tissues in vitro in the visible and near infrared spectral range. *Physics in Medicine and Biology* **47**, 2059–2073 (2002).

14. Jacques, S. L., Optical properties of biological tissues: A review (Physics in Medicine and Biology (2013) 58). *Physics in Medicine and Biology* **58**, 5007–5008 (2013).

15. Tanimoto, Y., et al., Calcium dynamics regulating the timing of decision-making in C. Elegans. *eLife* **6**, 1–30 (2017).

16. Marshel, J. H., et al., Cortical layer–specific critical dynamics triggering perception. *Science* **365**, eaaw5202 (2019).

17. Oh, Y., et al., An orange calcium-modulated bioluminescent indicator for non-invasive activity imaging. *Nature Chemical Biology* **15**, 433–436 (2019).

18. Bergs, A., et al., Rhodopsin optogenetic toolbox v2.0 for light-sensitive excitation and inhibition in Caenorhabditis elegans. *PLoS ONE* **13**, 1–24 (2018).

19. Sun, J., Singh, V., Kajino-Sakamoto, R., Aballay, A., Neuronal GPCR controls innate immunity by regulating noncanonical unfolded protein response genes. *Science* **332**, 729–732 (2011).

20. Rajaee, M., Ow, D. W., A new location to split Cre recombinase for protein fragment complementation. *Plant Biotechnology Journal* **15**, 1420–1428 (2017).

21. Troemel, E. R., Chou, J. H., Dwyer, N. D., Colbert, H. A., Bargmann, C. I., Divergent seven transmembrane receptors are candidate chemosensory receptors in C. elegans. *Cell* **83**, 207–218 (1995).

22. Schmitt, C., Schultheis, C., Husson, S. J., Liewald, J. F., Gottschalk, A., Specific Expression of Channelrhodopsin-2 in Single Neurons of Caenorhabditis elegans. *PLoS ONE* **7**, e43164 (2012).

23. Kaplan, J. M., Horvitz, H. R., A dual mechanosensory and chemosensory neuron in Caenorhabditis elegans. *Proceedings of the National Academy of Sciences of the United States of America* **90**, 2227–2231 (1993).

24. Bany, I. A., Dong, M. Q., Koelle, M. R., Genetic and cellular basis for acetylcholine inhibition of Caenorhabditis elegans egg-laying behavior. *Journal of Neuroscience* **23**, 8060–8069 (2003).

25. Kopchock, R. J., Ravi, B., Bode, A., Collins, K. M., The Sex-Specific VC Neurons Are Mechanically Activated Motor Neurons That Facilitate Serotonin-Induced Egg Laying in C. elegans. *The Journal of neuroscience* **41**, 3635–3650 (2021).

26. Collins, K. M., et al., Activity of the C. elegans egg-laying behavior circuit is controlled by competing activation and feedback inhibition. *eLife* **5**, 1–24 (2016).

27. Banerjee, N., Bhattacharya, R., Gorczyca, M., Collins, K. M., Francis, M. M., Local neuropeptide signaling modulates serotonergic transmission to shape the temporal organization of C. elegans egg-laying behavior. *PLoS Genetics* **13** (2017).

28. Zhang, M., Schafer, W. R., Breitling, R., A circuit model of the temporal pattern generator of Caenorhabditis egg-laying behavior. *BMC Systems Biology* **4** (2010).

29. Jose, A. M., Bany, I. A., Chase, D. L., Koelle, M. R., A specific subset of transient receptor potential vanilloid-type channel subunits in Caenorhabditis elegans endocrine cells function as mixed heteromers to promote neurotransmitter release. *Genetics* **175**, 93–105 (2007).

30. Fernandez, R. W., et al., Cellular Expression and Functional Roles of All 26 Neurotransmitter GPCRs in the C. elegans Egg-Laying Circuit . *The Journal of Neuroscience* **40**, 7475–7488 (2020).

31. Jewell, S., Witten, D., Exact spike train inference via 0 optimization. *Annals of Applied Statistics* **12**, 2457–2482 (2018).

32. Frøkjær-Jensen, C., et al., Single copy insertion of transgenes in C. elegans. *Nat. Genet.* **40**, 1375–1383 (2008).

33. Bendena, W. G., et al., A Caenorhabditis elegans allatostatin/galanin-like receptor NPR-9 inhibits local search behavior in response to feeding cues. *Proceedings of the National Academy of Sciences of the United States of America* **105**, 1339–1342 (2008).

34. Collins, K. M., Koelle, M. R., Postsynaptic ERG potassium channels limit muscle excitability to allow distinct egg-laying behavior states in caenorhabditis elegans. *Journal of Neuroscience* **33**, 761–775 (2013).

35. Dickinson, D. J., Pani, A. M., Heppert, J. K., Higgins, C. D., Streamlined genome engineering with a self-excising drug selection cassette. *Genetics* 1–33 (2015).

36. Sengupta, P., Colbert, H. A., Bargmann, C. I., The C. elegans gene odr-7 encodes an olfactory-specific member of the nuclear receptor superfamily. *Cell* **79**, 971–980 (1994).

37. Emtage, L., et al., IRK-1 potassium channels mediate peptidergic inhibition of Caenorhabditis elegans serotonin neurons via a Go signaling pathway. *Journal of Neuroscience* **32**, 16285–16295 (2012).

38. Johnston, I. D., McCluskey, D. K., Tan, C. K. L., Tracey, M. C., Mechanical characterization of bulk Sylgard 184 for microfluidics and microengineering. *Journal of Micromechanics and Microengineering* **24**, 035017 (2014).

39. Nagel, G., et al., Light activation of Channelrhodopsin-2 in excitable cells of caenorhabditis elegans triggers rapid behavioral responses. *Current Biology* **15**, 2279–2284 (2005).

40. Krieg, M., Dunn, A. R., Goodman, M. B., Mechanical control of the sense of touch by β-spectrin. *Nature Cell Biology* **16**, 224–233 (2014).

41. Baillargeon, P., et al., Design of Microplate-Compatible Illumination Panels for a Semiautomated Benchtop Pipetting System. *SLAS Technology* **24**, 399–407 (2019).

42. Jewell, S. W., Hocking, T. D., Fearnhead, P., Witten, D. M., Fast nonconvex deconvolution of calcium imaging data. *Biostatistics* **21**, 709–726 (2020).

43. Vogelstein, J. T., et al., Fast nonnegative deconvolution for spike train inference from population calcium imaging. *Journal of Neurophysiology* **104**, 3691–3704 (2010).

44. de Vries, S. E., et al., A large-scale standardized physiological survey reveals functional organization of the mouse visual cortex. *Nature Neuroscience* **23**, 138–151 (2020).

45. Taylor, S. R., et al., Molecular topography of an entire nervous system. *Cell* **184**, 1–19 (2021).